AGU PUBLICATIONS

JGR

Journal of Geophysical Research: Planets

RESEARCH ARTICLE
10.1002/2017JE005308

Key Points:
- We investigate magnitude, average spatial structure, and temporal variability of Mars' external magnetic field
- We identify periodic signals that can be used as inducing fields for future magnetic sounding
- Neutral winds are important drivers of ionospheric currents and associated magnetic fields

Correspondence to:
A. Mittelholz,
amittelh@eos.ubc.ca

Citation:
Mittelholz, A., C. L. Johnson, and R. J. Lillis (2017), Global-scale external magnetic fields at Mars measured at satellite altitude, *J. Geophys. Res. Planets*, *122*, 1243–1257, doi:10.1002/2017JE005308.

Received 17 MAR 2017
Accepted 18 MAY 2017
Accepted article online 23 MAY 2017
Published online 15 JUN 2017

Global-scale external magnetic fields at Mars measured at satellite altitude

A. Mittelholz[1], C. L. Johnson[1,2], and R. J. Lillis[3]

[1]Department of Earth, Ocean and Atmospheric Sciences, University of British Columbia, Vancouver, British Columbia, Canada, [2]Planetary Science Institute, Tucson, Arizona, USA, [3]UC Berkeley Space Sciences Laboratory, Berkeley, California, USA

Abstract The Martian magnetic field is unique among those of the terrestrial planets. It is the net result of the interaction of the solar wind and the interplanetary magnetic field (IMF) with crustal remnant magnetization and a planetary ionosphere. Internal fields of crustal origin have been the subject of extensive studies; the focus of our work is identification and characterization of contributions from external magnetic fields using the Mars Global Surveyor (MGS) vector magnetic field data. We investigate the magnitude, average spatial structure, and temporal variability of the external magnetic field at MGS mapping altitude of 400 km by first subtracting the expected contributions from crustal fields using existing global crustal field models. We identify periodicities and spatial structure in the field related to the day-night cycle and Carrington rotations, as well as variations corresponding to an annual cycle and short aperiodic signals. We suggest that ionospheric currents driven by upper atmosphere winds contribute to the observed zonal structure in the daily variation in the external magnetic field. Finally, we discuss the potential for magnetic sounding studies using time-varying external fields and surface magnetometry measurements from the InSight mission to be launched in 2018.

1. Introduction

The Martian magnetic field environment is a result of interactions among the internal crustal field and external fields, including the interplanetary magnetic field (IMF) and fields generated by ionospheric currents. Mars' magnetic fields have been measured by fluxgate magnetometers on the Mars Global Surveyor (MGS) and Mars Atmosphere and Volatile Evolution Mission (MAVEN) missions.

MGS operated in orbit from 1997 to 2006 [*Acuña et al.*, 1999]. It confirmed the lack of a current internal dynamo field and provided the first detection of strong crustal magnetization [*Acuña et al.*, 1998]. Crustal magnetization is concentrated in the southern hemisphere, especially in the ancient Noachian terrains of Terra Sirenum and Terra Cimmeria [*Acuña et al.*, 1999]. The crustal field comprises the dominant contribution to the measured magnetic field at MGS altitudes of ~100 km up to at least ~400 km [*Brain et al.*, 2003], and its amplitude exceeds that at Earth by up to an order of magnitude, indicating strong remanent magnetization, large volumes of coherently magnetized crust, or a combination of both [e.g., *Connerney et al.*, 1999; *Purucker et al.*, 2000]. The dense coverage provided by MGS data enabled global spherical harmonic [e.g., *Arkani-Hamed*, 2001, 2002; *Cain*, 2003; *Morschhauser et al.*, 2014], local spherical harmonic [*Plattner and Simons*, 2015], spherical cap [*Voorhies et al.*, 2002; *Voorhies*, 2008], and equivalent source dipole models [e.g., *Purucker et al.*, 2000; *Langlais et al.*, 2004] to be developed for the crustal field.

In contrast, the global-scale external field has received less attention. The external field is a complex field, both temporally (e.g., solar wind conditions, day/night, and season) and spatially (e.g., interaction with crustal fields) with past studies falling into two broad categories:

The first category of studies addressed interactions of the interplanetary magnetic field (IMF) with the Martian obstacle including the ionosphere and crustal field. These studies typically focused on regional subsets of the data rather than global analyses. The interaction of the IMF with crustal fields, specifically the dependence of the magnetic field on altitude, solar zenith angle, and planetary location using MGS data, has been described by *Brain et al.* [2003]. In a distinct study [*Brain et al.*, 2006] the dayside magnetic field direction at 50°–60°N latitude, below the magnetic pileup boundary (MPB), was found to be dependent on IMF polarity sector. The field just below the MPB is referred to as a "draped field" or "draped IMF", as it drapes around the dayside of

the planet. As such, it would be expected to reflect the bimodal distribution of IMF directions (i.e., toward and away from the Sun) experienced by MGS that results from the periodic change in position of Mars with respect to the heliospheric current sheet. However, an asymmetry in draping direction was observed, reflected by a strongly preferred draping direction when Mars is in one IMF polarity sector and a less strongly preferred (opposite) direction in the sector with the opposite polarity. The reason for this was unknown, but ideas proposed included field lines preferentially accessing the ionosphere for one upstream IMF configuration, or global effects related to crustal field modification of the interaction with the solar wind [*Brain et al.*, 2006]. In contrast, the nightside external field was observed to be quieter than the daytime field and is well described by the draping of the IMF field [*Ferguson et al.*, 2005]. *Ferguson et al.* [2005] also observed a bimodal distribution in the *x* component of the magnetic field on the nightside. As the ionosphere results from solar wind ionization of the upper atmosphere, it is intuitive that solar wind conditions influence the dayside external field and events like coronal mass ejections and stream interaction regions lead to strongly enhanced external fields. Furthermore, complex interactions of external fields with heterogeneously distributed crustal fields have been observed [e.g., *Brain et al.*, 2003; *Lillis and Brain*, 2013]. Crustal fields exert magnetic pressure and contribute to the Martian obstacle to the solar wind, locally pushing the MPB outward [*Crider et al.*, 2003]. Crustal magnetic field lines can also reconnect with external fields depending on the IMF conditions [*Brain et al.*, 2006; *Eastwood et al.*, 2008; *Halekas and Brain*, 2010]. These interactions mean that both the planetocentric body-fixed and solar orbital frames are important in determining the resulting magnetic field structure.

The second group of external field studies has focused on descriptions or models that are purely mathematical and that serve the purpose of characterizing non-internal sources to facilitate or improve crustal field models. These models are global descriptions of an external field that is assumed to be static. A 9-month subset of MGS data was used by *Olsen et al.* [2010] to derive spherical harmonic expansions for the time-averaged internal, toroidal, and external fields, where internal fields are below and external fields are above the spacecraft at ~400 km altitude. More recently, while solving for a spherical harmonic crustal field model, *Morschhauser et al.* [2014] also estimated the spatial structure in the external field, under the assumption that all non-crustal fields originate from sources above spacecraft altitudes. These models offer a global but time-averaged picture of a very dynamic environment.

In this study, we use MGS vector magnetic field data [*Acuña et al.*, 2001] to investigate the large-scale geometry, temporal variability, and magnitude of the external field at 400 km altitude. After introducing the data set and methodology, we focus on the daily and 26-day (Carrington solar rotation) cycle and examine any evidence for longer periodicities, related to the annual and solar cycle, as well as short aperiodic signals. We discuss persistent global structure observed in the external field and investigate possible physical explanations for it. Finally, we discuss the possibility of using the periodic signals in the external field for future magnetic sounding studies of interior electrical conductivity.

2. MGS Data Set Overview

MGS magnetic field data were mainly obtained during the mapping orbit (MO) phase of the mission [*Acuña et al.*, 2001] from 1999 to 2006. The orbit was near circular (altitudes 386 to 438 km), near polar (93° inclination), and Sun-synchronous, crossing the equator at 2 am and 2 pm, and provided global coverage at most latitudes in the Mars body-fixed frame (MBF). The radial component of the field (B_r) for the day and night time-averaged MO data from May 2000 to November 2006 is shown in Figure 1, together with the times series of all three vector field components for five example orbits. The global structure in B_r at 400 km altitude is similar for daytime and nighttime data (Figures 1a and 1b) and is well matched by the signal predicted from two crustal field models (Figures 1c [*Langlais et al.*, 2004, hereafter L04] and 1d [*Morschhauser et al.*, 2014, hereafter M14]). L04 and M14 are available as degree and order 90 (L04) and 110 (M14) spherical harmonic models corresponding to spatial resolutions of 237 and 194 km, respectively, at the surface of Mars. The two models differ in the data used, and in the model construction; however, differences between them are negligible at 400 km altitude.

The crustal magnetic field is the dominant contribution to the measured field at spacecraft altitude over many regions and the influence of the external field is relatively weak when averaged over a long time interval. The five individual orbits shown in Figure 1 illustrate the dependence of the magnetic field component on geography and local time. The magnetic fields show increased magnitudes during the daytime compared with the nighttime. Day-night variations are caused by external fields evidenced mostly in the horizontal components B_θ and B_φ. In contrast, even on the dayside the amplitude of B_r is low except in the vicinity of crustal fields.

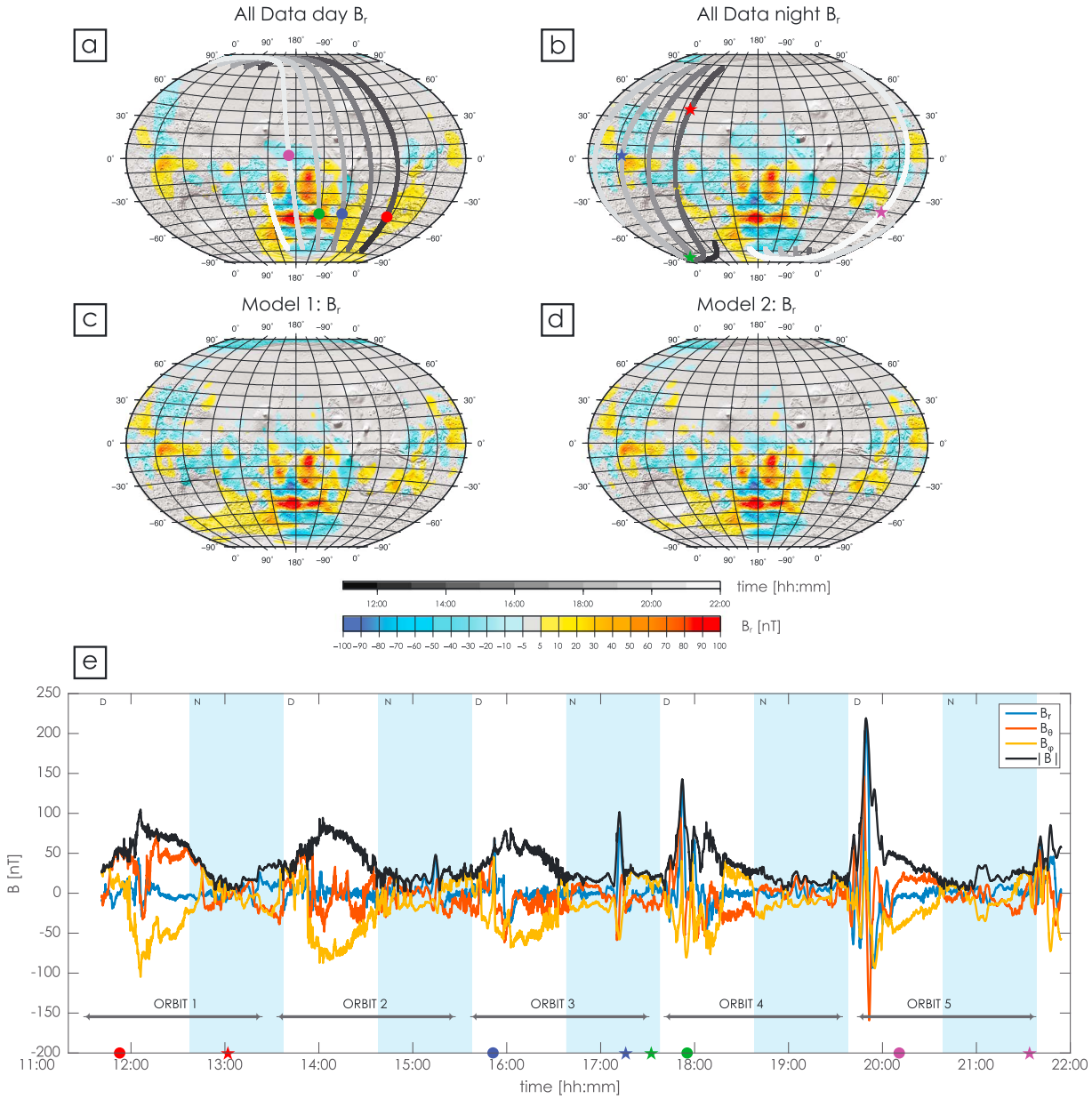

Figure 1. Radial component of the magnetic field, B_r, averaged over the period 2000–2006 for (a) daytime and (b) nighttime. Observation altitudes were 386–438 km. Tracks for the five orbits in Figure 1e are shown with the grey colorbar indicating time in hours along the orbit track. The predicted B_r at 400 km altitude from the crustal field models of (c) *Langlais et al.* [2004] and (d) *Morschhauser et al.* [2014]. (e) The magnetic field components and strength (|B|) from the five orbits from 10 April 2003 whose tracks are shown in Figures 1a and 1b. Blue shading highlights nightside segments of the orbits. Circles and stars along the track indicate specific times (Figure 1e) and locations (Figures 1a and 1b) of sections of the orbits discussed in the text.

The dayside tracks of orbits one and two pass over weaker crustal fields than the dayside tracks of orbits four and five (Figure 1a). Crustal field contributions are clearly visible when regions of strong crustal magnetization are crossed during the nighttime, e.g., in orbit three just after 17:00 h, and during the daytime, e.g., in orbits four and five (Figures 1a, 1b, and 1e). Figure 1 shows that although crustal fields dominate B_r at mapping altitudes, there are clear signatures of external fields that have a daily periodicity as well as higher-frequency variability.

We investigate external fields using MGS MO data. We do not use Aerobraking (AB) and Science Phasing Orbit (SPO) data, because although altitudes as low as 80 km were reached [*Acuña et al.*, 2001], the local time and altitude coverage during the AB and SPO phases were sparse and very heterogeneous. Although this has

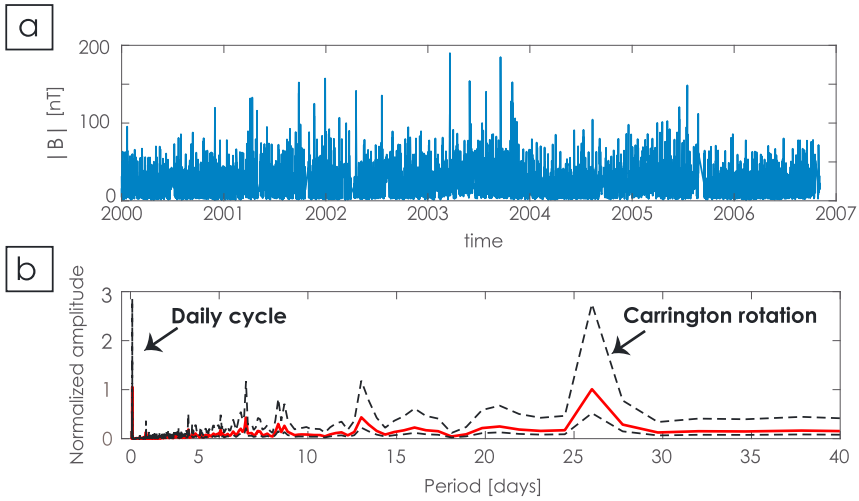

Figure 2. (a) The magnetic field strength |B| for the MGS MO phase spanning approximately 3 Martian years. The median value from each orbit for the latitude band 50°–60°N is shown. (b) The amplitude spectrum (red) and the 95% confidence bounds (dashed black) of the time series in Figure 2a normalized by the maximum value of the spectrum, the daily peak. Clear peaks at several periods are seen: The daily signal appears with an apparent period close to the MGS orbital period. The 26-day peak corresponds to the average synodic solar rotation period (Carrington rotations). The first harmonic at around 13 days is also seen.

been somewhat improved with the advent of MAVEN data, MGS MO data still provides the only data set with repeated coverage at consistent altitudes and local times over several Martian years. We use the M14 crustal field model to predict crustal fields along the orbit tracks and then subtract these from the observed vector magnetic field data. We analyze the residual field that comprises mainly of external fields including any contributions from the draped IMF and the ionosphere. Figure 1 and additional analyses by us confirm that the choice of crustal field model does not affect our results for external field properties at MO altitudes. We start by analyzing the data in the Mars Solar Orbital (MSO) coordinate system in which $\hat{x}$ points toward the Sun, $\hat{z}$ is normal to the plane of Mars' orbit, and $\hat{y}$ completes the right-handed coordinate system. This frame is useful for studying phenomena controlled by Mars' interaction with solar drivers, i.e., solar photon flux or solar wind while neglecting any interactions controlled by effects tied to the body-fixed frame, such as crustal fields.

3. Spatial and Temporal Variability

The external magnetic field exhibits both aperiodic and periodic signals. Aperiodic signals, such as the orbit-to-orbit variations and higher-frequency signals seen in Figure 1, depend on several factors such as solar wind conditions and crustal fields. We focus on periodic signals that can be related to known physical processes. Figure 2a shows the time series of the magnitude of the external field, $|B|$, at 50°–60°N latitude. We chose this region because there are no crustal field signals at MO altitudes (Figures 1a–1d), and it was previously examined in *Brain et al.* [2006]. The local times of the tracks crossings the latitude band are about 16:00 h and 02:00 h. The corresponding amplitude spectrum and associated confidence limits, computed using Welch's method (Figure 2b), show peaks corresponding to periods of a Martian day and 26 days. There is some suggestion of modulation of $|B|$ in Figure 2a at a period of a Martian year.

The 26-day cycle corresponds to the average synodic solar rotation period of Mars, τ_{Cr}, the Carrington rotation, equal to 26.35 days. We observe a broad peak at around 26 days with variable amplitude (seen by the 95% confidence bounds). This is related to variations in timing of the heliospheric current sheet crossing which depends on several factors, such as solar activity [e.g., *Owens and Forsyth*, 2013]. We observe peaks at τ_{Cr}/n, where n is an integer, the harmonics of the period τ_{Cr}. The maximum amplitude in the spectrum is associated with a clearly defined daily period, corresponding to the day-night variations in Figure 1. In the following we conduct a more detailed analysis of these two cycles.

3.1. The 26-Day Cycle

We first examine the 26-day cycle to identify clear contributions to the external field from the IMF. We filter the daytime data at 50°–60°N by taking the running median of $|B|$ over 6 days and 4 months (Figure 3). The 6 day

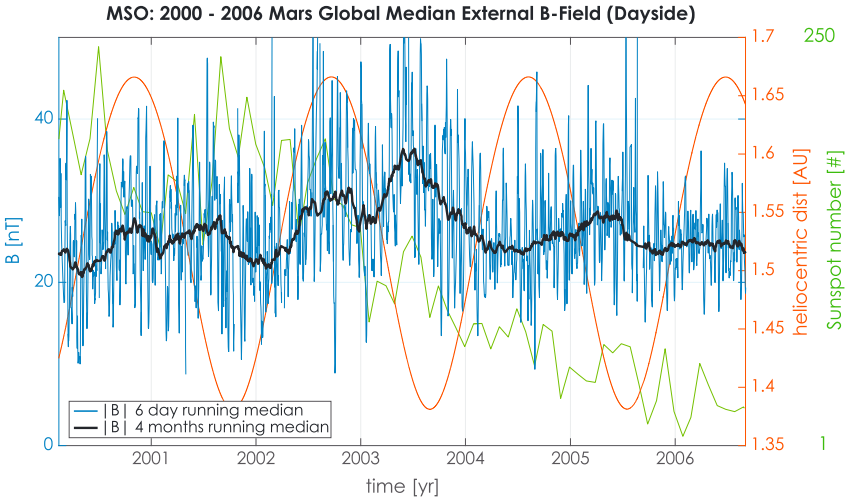

Figure 3. The 6 day (blue) and 4 month (black) running median for daytime $|B|$ in the latitude band 50°–60°N after subtraction of crustal field model M14. The heliospheric distance (red) and sunspot number (green) are also shown.

running median window length was chosen to remove the daily signal and higher-frequency variations but retain signals at τ_{Cr} and its first harmonic. Figure 2b shows that there is little power in the spectrum at periods between 1 and 13 days, so the precise choice of window length (e.g., 5 or 7 days versus 6 days) is unimportant. The Carrington 26-day cycle is seen in the 6-day running median but, as expected, is no longer visible in the 4-month running median. The 4-month running median was chosen to remove signals at τ_{Cr} but retain any possible seasonal signal, and indeed, the result suggests a possible weak annual cycle, equivalent to 687 days. For each Martian year, a peak in $|B|$ is observed shortly before perihelion, when Mars is closest to the Sun. Secondary peaks sometimes occur at or near times of aphelion. Figure 3 shows no obvious correlation of $|B|$

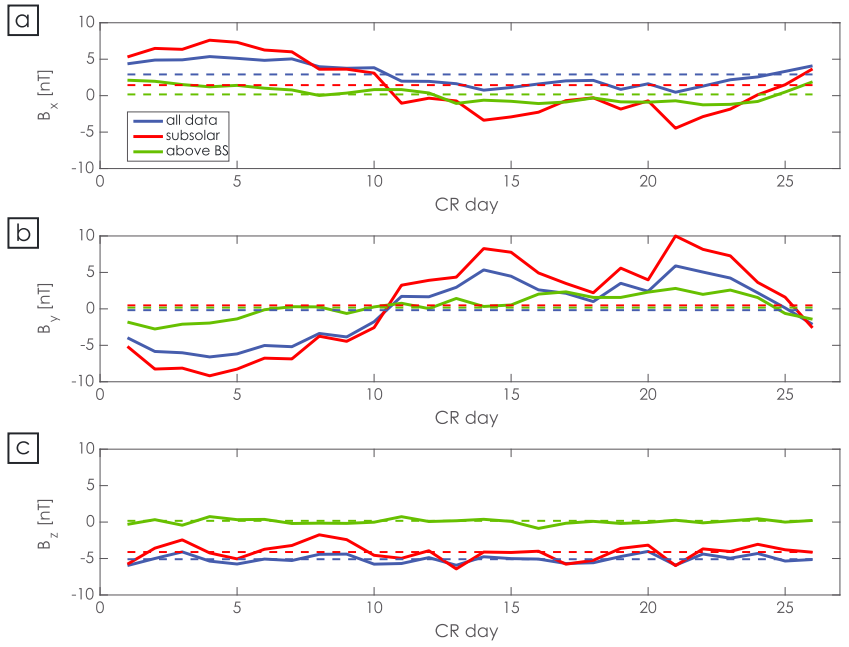

Figure 4. The global (blue) and subsolar (red) mean of MGS data binned in 26 data sets corresponding to day 1 to day 26 of a Carrington rotation for all B components in MSO. Additionally, we show dayside MAVEN data above the bow shock (green) binned in the same manner from October 2014 to February 2016. Dashed lines show the mean value for each data set. Day 1 of the Carrington cycle is arbitrarily defined. Each stacked Carrington rotation day contains ~91 Earth days of data with ~12 orbits per Earth day providing ~1100 orbits. The 95% confidence intervals in the stacked signals for all components are ~ ±1.2 nT.

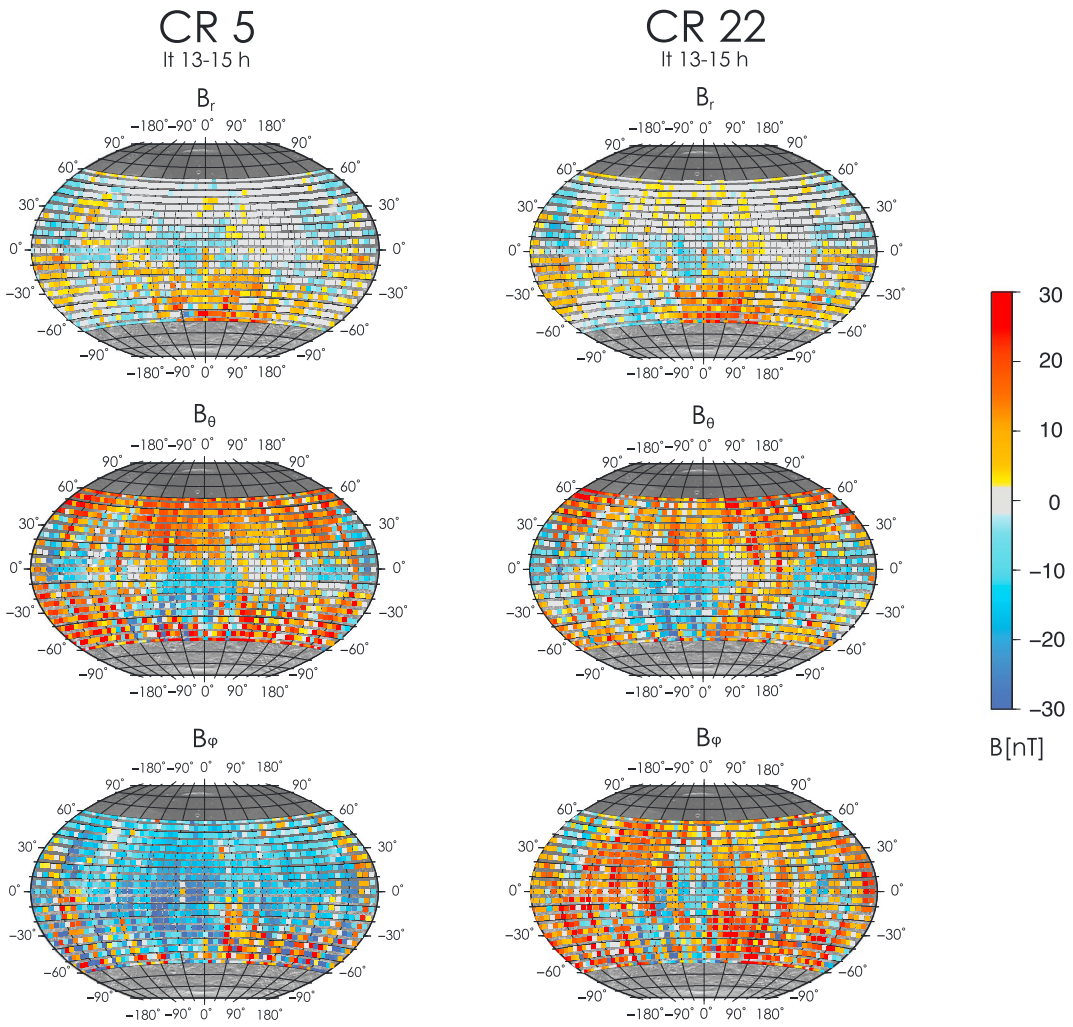

Figure 5. The global quasi-static magnetic field in the MBF frame for Carrington rotation days 5 and 22 after subtraction of the internal crustal field [*Morschhauser et al.*, 2014] for daytime data (local time 13–15 h). Median values for all *B* components in 6° × 6° bins for MGS mapping orbit data from 2000 to 2006. We exclude data poleward of 60°, because at these latitudes sampling occurs over a variety of local times and is biased in season.

with solar activity at periods of 6 days and longer. However, the limited time interval spanned by the MGS data does not allow further examination of any influence of the solar cycle. Having identified a cycle related to the 26.35 day period, we bin the data in 26 data sets corresponding to distinct days (1 through 26) of the Carrington cycle. We examine the B_x, B_y, and B_z components (Figures 4a–4c, respectively) in MSO coordinates and calculate a mean global value and a mean value within ± 20° latitude of the subsolar point for each of the 26 data sets. Furthermore, we follow the same procedure with MAVEN data from October 2014 to August 2015 specifically selecting daytime data outside the bow shock (distance from center of the planet is greater than $2.5R_{Mars}$) to obtain an estimate of the uncompressed IMF as a function of Carrington cycle day. Day 1 of the cycle is arbitrarily defined for both time intervals.

For data taken above (MAVEN) and below (MGS) the bow shock, we observe some characteristics of a magnetic field dominated by contributions from the IMF. The expected polarity changes during the 26-day cycle are visible in B_y and somewhat in B_x but are not, however, observed in B_z. The MAVEN data record the magnitude and direction of the IMF expected at Mars. MGS MO data show larger amplitude periodic signals in B_x and B_y, compared with the MAVEN data taken outside the bow shock. These likely reflect the increase in magnitude of the field associated with a compressed IMF below the bow shock.

The polarity change in B_y is in agreement with earlier studies. For example, in a study by *Civet and Tarits* [2014], the extrapolated Advanced Composition Explorer [*Stone et al.*, 1998] IMF field was used as a proxy for external

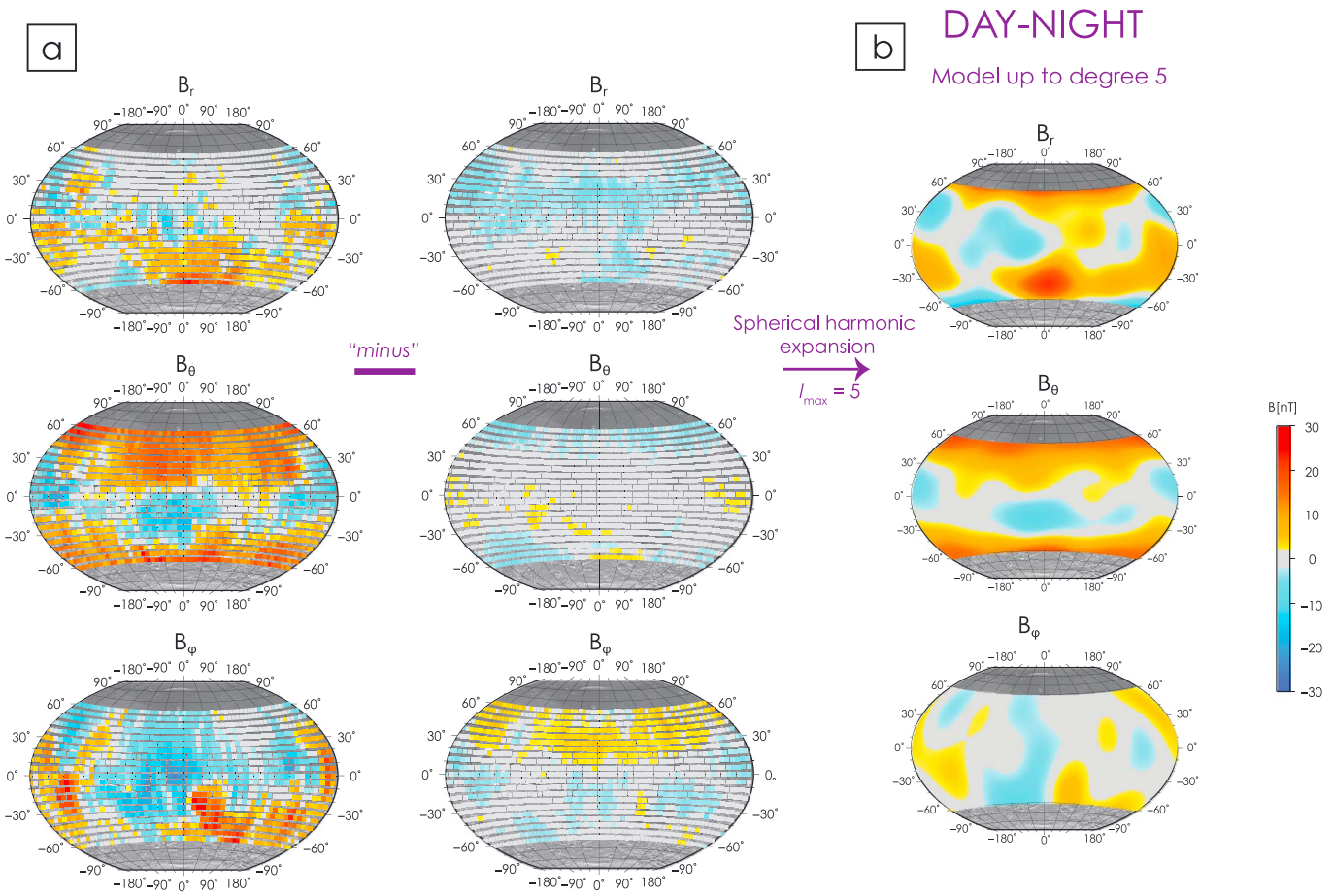

Figure 6. (a) The global quasi-static magnetic field for 2000–2006 after subtraction of the internal crustal field [*Morschhauser et al.*, 2014] for day (local time 13–15 h, left column) and night (local time 1-3 h, right column) in MBF. The median values are shown in 6° × 6° bins. We exclude data poleward of 60°, because at these latitudes sampling occurs over a variety of local times and is biased in season. (b) Predictions of a degree and order 5 spherical harmonic model for the day-night difference in the field, plotted at 400 km altitude.

field variability at Mars and it was found that only the B_y component of the IMF proxy and the MGS data set were significantly correlated. However, both this previous study and our Figure 4 suggest that B_x and B_z are affected by sources other than the IMF. Above the bow shock, the mean values of B_x, B_y, and B_z are approximately zero over the 26-day cycle, but at MO altitudes the mean B_x and B_z are non-zero, both for the globally averaged data and for data confined to a region near the subsolar location.

To investigate possible contributions to the field other than the IMF, we next analyze the data in the Mars body-fixed frame (MBF). This allows us to examine, e.g., fields that might result from the interaction of crustal field lines with the IMF.

In Figure 5 we show global maps of the data binned in 6° × 6° latitude and longitude bins for days 5 and 22 of the cycle. The data are plotted from −60° to 60° as the 2 A.M./2 P.M. orbit allows for homogeneous local time sampling around the equator. We use only data between 1–3 h and 13–15 h to create a snapshot of the external field for this time frame. We exclude regions poleward of 60° latitude, as the poles are sampled at a variety of local times with coverage depending on season; e.g., during northern hemisphere summer daytime sampling would only occur at the north pole whereas the south pole would contain nighttime measurements.

The horizontal component B_φ (east-west component) shows an overall change in polarity between days 5 and 22 as expected for a field generated mainly by the IMF and consistent with the B_y (with or against Mars' orbital motion) signal in the MO data (Figure 4). The change in polarity is consistent with the mean signal of zero in Figure 4. However, an average zonal structure characterizes B_θ in both days 5 and 22, with dominantly southward (positive) B_θ at midlatitudes. This is consistent with the globally averaged B_z in Figure 4.

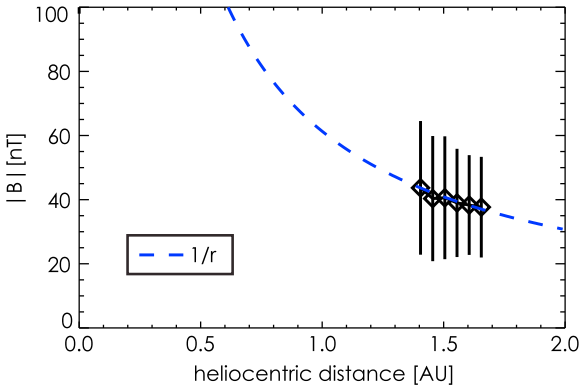

Figure 7. Dayside $|B|$ at 50°–60°N MSO latitude versus heliocentric distance, r, in AU. Error bars indicate the standard deviation in $|B|$ in each heliocentric bin. $|B|$ values estimated from the MGS MO data, spanning 3 Martian years. The dashed blue line shows a $1/r$ relationship that matches the observations well.

We observe spatial structure in B_r for both days in the cycle with large amplitudes associated with regions of strong crustal magnetization. The B_r component does not exhibit a polarity change consistent with the non-zero mean residual signals in B_x and B_z observed in Figure 4. Overall, the observations are consistent with inferences from previous studies of external fields that comprise a draped IMF field which mostly affects horizontal components and a radial field reflecting interaction with crustal fields [e.g., *Brain et al.*, 2003]. However, the observed zonal structure in B_θ seen in the body-fixed frame has not been previously reported.

3.2. Daily Cycle

In order to investigate any spatial structure in the daily variation in the external field, we bin the daytime and nighttime MO residuals as above but take the median of the whole data set from 2000 to 2006 in each geographic bin (Figure 6). Consistent with the results in Figures 4 and 5, we observe a time-averaged field with persistent spatial structure. The larger data volume leads to a smoother picture of the average field compared with that in Figure 5 for which only 1/26 of the data set is used in each plot. Opposite polarity structure related to Carrington rotations should be averaged out in Figure 6, so any remaining structure is related to possible asymmetries resulting from the IMF interaction with the Martian obstacle [e.g., *Brain et al.*, 2006] and/or fields due to other current sources.

As expected, the daytime and nighttime signals show different behavior. The nighttime field is very quiet, whereas the daytime field can have an average amplitude in excess of 30 nT. The daytime radial component, B_r, in the external field appears to be correlated with crustal fields (see section 4), even after subtraction of predicted crustal field values at mapping altitude as observed in Figure 5. This likely reflects the interaction of external and internal fields and compression on the crustal fields on the dayside [e.g., *Brain et al.*, 2003]. The horizontal components B_θ and B_φ show larger field amplitudes compared to the radial component. B_θ, the colatitudinal component, exhibits a zonal structure similar to that seen over shorter time intervals (Figure 5). B_φ, the longitudinal component, varies geographically.

3.3. Longer and Shorter Timescales

Analysis of the annual cycle is limited by the only ~3 Mars years of MGS MO data. However, daytime data averaged in the latitude band between 50° and 60° and binned as a function of heliospheric distance show that the magnitude of the field falls off with $1/r$, the expected dependence from a fluid solar wind model (Figure 7). This confirms the previous work that shows that the magnetic pressure is the dominant term below the MPB, balancing the solar wind pressure [*Crider et al.*, 2003]. Proximity to the Sun (seasonal cycle) causes an increase in solar wind pressure and therefore an overall increase in $|B|$. Additionally, by using the magnetic field as a solar wind pressure proxy [*Crider et al.*, 2003], we can infer that solar events, fluctuations of solar wind pressure, will cause aperiodic variations in the external field.

4. Discussion

4.1. Global Spatial Pattern of the Averaged External Field

External fields, viewed in the MSO frame (Figure 4, B_x and B_y) and the MBF frame (Figure 5, B_θ, and in particular B_φ) record changes in sign consistent with the change in polarity in the IMF at Mars expected approximately every 13 days. Over long time scales, i.e., many 26 day periods, the field resulting from these polarity changes should average to zero, but Figure 6 shows persistent dayside structure in all three components of the magnetic field. Here we further assess that structure and its possible causes.

Motivated by previous studies that have reported modification of the magnetic field environment at MO altitudes over crustal fields [e.g., *Brain et al.*, 2003; *Lillis and Brain*, 2013], we first assess any correlation of structure in the external field with crustal fields. As expected, after the subtraction of crustal fields predicted by current

models (M14 or L04), residual fields averaged over many IMF cycles are very small in amplitude on the nightside. In contrast on the dayside, external field structure in B_r, and to some extent in B_φ (Figure 6), appears to qualitatively be correlated with regions of strong crustal fields (Figure 1). We compare the daytime averaged external field (Figure 6) with predictions of the crustal magnetic field models M14 and L04 (Figures 1c and 1d) at 400 km altitude, using a 12° by 12° grid to assess correlations at wavelengths easily resolved by the crustal field models at this altitude. Correlation coefficients of 0.53, −0.08, and 0.11 are obtained for $|B_{r,\mathrm{ext}}|$, $|B_{\theta,\mathrm{ext}}|$, and $|B_{\varphi,\mathrm{ext}}|$ with $|B_{r,\mathrm{M14}}|$, $|B_{\theta,\mathrm{M14}}|$, and $|B_{\varphi,\mathrm{M14}}|$, respectively. As expected from Figure 6, B_r shows the highest correlation with crustal fields, B_φ shows some modest correlation, and B_θ shows almost none. The correlations coefficients for $|B_r|$ and $|B_\varphi|$ allow the hypothesis that the external and crustal fields are uncorrelated to be rejected at the 99% confidence level. This is not true of B_θ, consistent with the qualitative result in the maps in Figure 6 cf. Figure 1. In other words, the radial and east-west components of the external fields are correlated to their crustal counterparts, but the north-south component is not.

We next assess possible explanations for the structure in the time-averaged external field that is not correlated with crustal fields. In particular, the B_θ component is dominated by large-scale zonal structure, both over the entire MGS sampling period (Figure 6), and also when only using subsets of the full data set (e.g., Figure 5). *Olsen et al.* [2010] also estimated a global model of the external field as mentioned in section 1. Their external field is a result of a spherical harmonic expansion where sources above the MGS mapping orbit (~400 km) are defined as external fields. This field is not directly comparable with our results as the latter represents the net non-crustal fields and thus include contributions from toroidal and external fields, as well as the part of the internal field which is not of lithospheric origin (e.g., the ionospheric field). However, we observe that the *Olsen et al.* [2010] nighttime external field is somewhat similar to our results consistent with weaker ionospheric contributions during the nighttime. The daytime external field differs, as ionospheric contributions and crustal field interaction are present in our residual signals and their amplitudes exceed the external fields modeled by *Olsen et al.* [2010].

The global structure may be related to the preferred draping direction of the field seen at 50°–60°N [*Brain et al.*, 2006] when MGS was in one solar wind sector. *Brain et al.* [2006] investigated several possible mechanisms for their observations but were unable to determine the root cause. Although some MHD simulations of the interaction of the solar wind with the Martian obstacle show asymmetries in the field strength and topology for different IMF polarities [*Brain et al.*, 2010], the persistent zonal structure in B_θ seen here has not previously been reported. We consider an alternative possibility for this structure: ionospheric currents driven by neutral winds in the Martian upper atmosphere.

Neutral winds have been shown to play an important role within the nighttime ionosphere [*Fillingim et al.*, 2012]. At Martian altitudes of 110–160 km, electrons and ions behave differently. For electrons the gyration frequency is higher than the collision frequency and so they gyrate about magnetic field lines more often than they collide with neutrals, i.e., they are "magnetized." The opposite is true for ions, whose motions are dominated by the neutral winds. This difference in motion leads to charge separation and currents. We investigate whether neutral winds could drive electric currents in the ionosphere that have a direction and magnitude consistent with the observed magnetic field structure.

Using a Mars global circulation model (MGCM) [*Forget et al.*, 1999; *Millour et al.*, 2015], we examine predicted winds in the N-S and E-W direction at 130 km altitude (the approximate ionospheric peak altitude at the subsolar point) averaged over all seasons (Figure 8). The MGCM includes the upper atmosphere and thermosphere up to ~350 km, is available as GUI tool, and source code can be requested via the Mars Global Climate Database (MCD) website (http://www-mars.lmd.jussieu.fr/mars/access.html). We used version 5.2 of the MCD for the analyses presented here.

The average annual wind field shows stronger horizontal winds at middle to high latitudes and very weak winds around the equator. In order to compare neutral winds and the magnetic field we highlight the sampling period of the magnetic data (2 A.M./P.M.). At middle to high latitudes, the main wind direction is eastward around 2 P.M. and westward to almost no east-west component around 2 A.M. Winds in the equatorial region are smaller in amplitude than at high latitudes at both 2 A.M. and 2 P.M. We expect little or no generation of ionospheric currents due to winds during the nighttime as a result of relatively weak ionization and therefore focus on the daytime field.

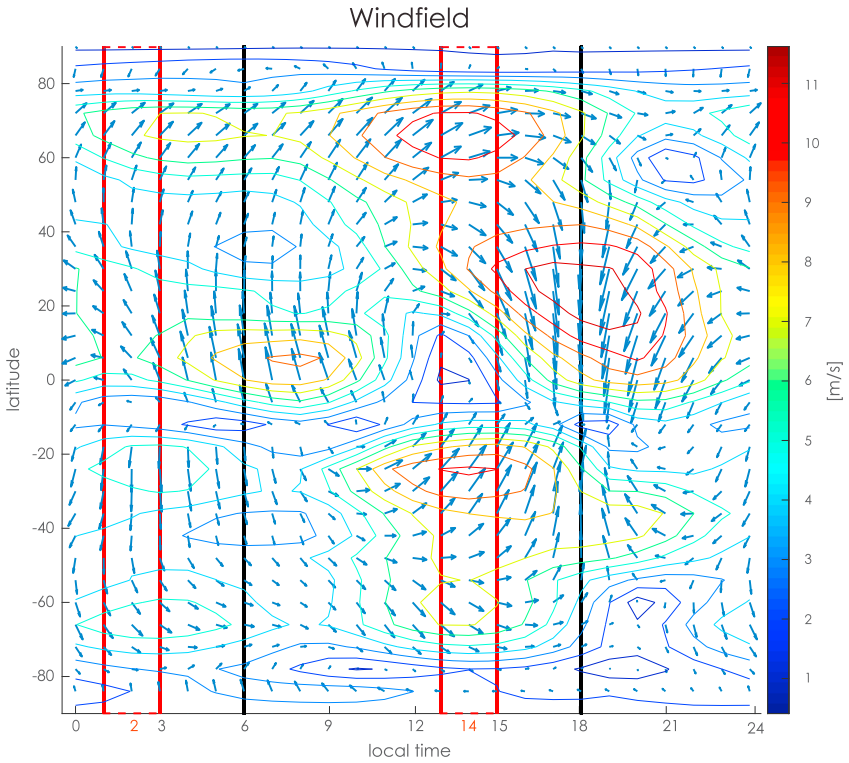

Figure 8. The global horizontal wind field for all local times, averaged over all seasons, predicted by a Mars Global Circulation Model [*Forget et al.*, 1999; *Millour et al.*, 2015] using 6° latitude bins. The red boxes highlight local times 1–3 and 13–15 h, the main sampling intervals for the MGS magnetic data. Black lines indicate dawn and dusk. The contour lines show the magnitude of the horizontal field; vectors give the directions, where the y-axis denotes the N-S direction and the x-axis the E-W direction.

During the day, the direction of modeled winds in middle to high latitudes is mainly eastward. Pedersen currents carry collisional ions in the direction of the applied force (the wind). This results in eastward currents and a southward directed magnetic field at spacecraft altitudes (i.e., above the ionosphere). This corresponds to a positive B_θ component at those latitudes in the northern and southern hemispheres, qualitatively consistent with the observed zonal pattern in B_θ. Winds in the equatorial region are very weak with no clear zonal structure, and the corresponding B_θ component of the magnetic field is also much weaker.

The longitudinally averaged horizontal wind and magnetic field components at 2 P.M. show the similar structure of the E-W wind field (Figure 9a) and the B_θ component (Figure 9c). At most latitudes, the averaged N-S component of the wind field is weaker (Figure 9b) and does not resemble the B_φ component of magnetic field (Figure 9d). To further test the hypothesis that winds could drive electric currents resulting in the observed structure in the magnetic fields, we calculated the magnetic field that would be produced assuming that at any given latitude ions move at the average E-W wind speed shown in Figure 9a. This results in a current density $j = nq(v_i - v_e)$, where q is the elementary charge, v_i and v_e the velocity of the ions and electrons, respectively, and n is the electron density. Electrons are assumed to be stationary as the ambient magnetic field is complex resulting in no substantial net motion of gyrating electrons. n is to be the approximate electron density as observed by MAVEN ($10^{11}/m^3$) at 130 km altitude and a solar zenith angle of 80° [*Vogt et al.*, 2016]. We modeled the magnetic field due to a line current in each 6° latitude band (~360 km), assuming a spacecraft distance of ~270 km (mapping orbit altitude) from the source (130 km altitude). Even with this simplified approach, the current generates a magnetic field that is the correct order of magnitude and that has a similar latitudinal structure to that seen in the MGS data (Figure 9c).

A secondary effect can be attributed to Hall Currents. Hall Currents are perpendicular to the applied force (wind) and the ambient magnetic field and thus depend on the local ambient magnetic field. At Mars this is complex and dynamic. For example, ambient magnetic fields perpendicular to an E-W wind field must be either radial or latitudinal. The current resulting from a radial magnetic field points N-S, generating a

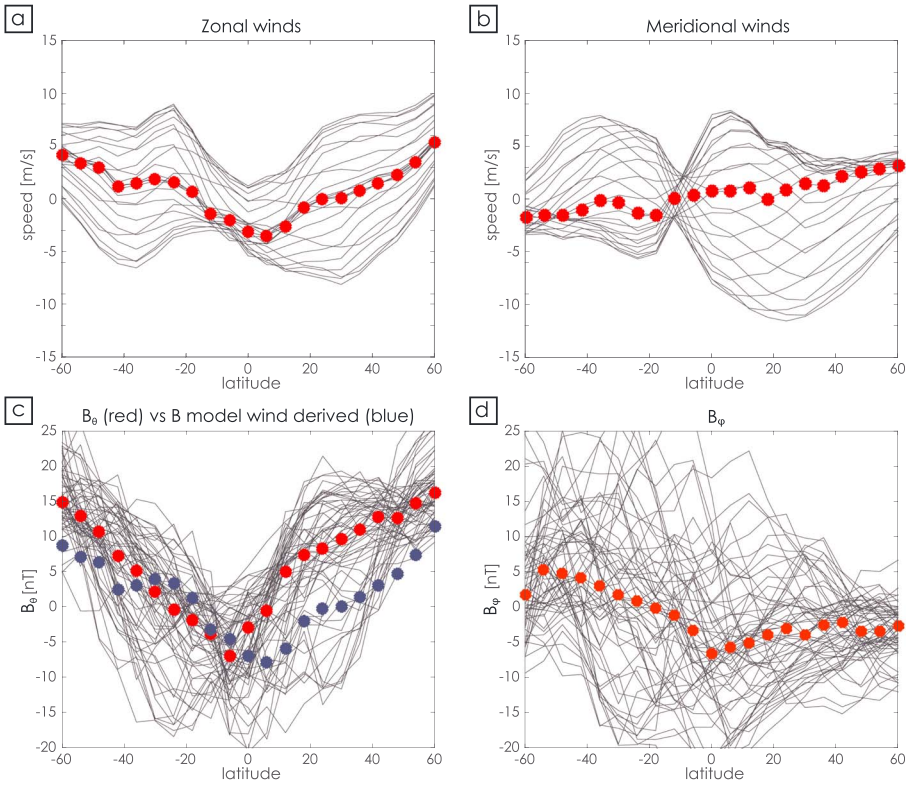

Figure 9. The latitudinal profiles of the averaged model field (binned in 6° × 6°) of (a) zonal and (b) meridional wind speeds and the magnetic (c) B_θ and (d) B_φ components of the binned MGS daytime data set as shown in Figure 6. The red dotted line shows the median of all latitude profiles (grey). The blue dotted line in Figure 9c represents the magnetic signal resulting from the zonal wind field of Figure 9a.

secondary magnetic field in the E-W (B_φ) and radial (B_r) direction. Similarly, E-W winds and an ambient latitudinal magnetic field (B_θ), would drive current systems in the radial direction, generating a horizontal secondary magnetic field (B_φ, B_θ). The strongest ambient magnetic fields will be in the regions of crustal fields as these are the major component of the overall field at 400 km altitude (Figure 1), and these regions experience substantial winds (Figure 8). Secondary magnetic fields will therefore mostly affect regions like Terra Cimmeria and Sirenum. Thus, Hall currents could contribute to the correlation of crustal and external fields.

On Earth we find a similar current system driven by ionospheric and thermospheric winds [*Chapman and Stagg*, 1929; *Yamazaki and Maute*, 2017]. The so-called solar quiet (Sq) current system generates a smoothly varying magnetic field at about 90–150 km altitude, in the near absence of solar wind-driven disturbances. The magnetic field shows a characteristic pattern with latitude that is symmetric about the magnetic equator. In our analyses (Figure 6), we take the median of the data in each MO data bin in order to exclude days of anomalous solar activity, and our representation is thus analogous to solar quiet days. Figure 6 shows the 2 A.M. and 2 P.M. average fields, which we suggest can be explained by an ionospheric current system. Both the Martian and Earth Sq current systems produce magnetic signals of tens of nanoteslas that are variable in time. For the Martian field, we are restricted in our analysis due to orbit geometry of MGS: The Sq current system is expected to be local time dependent but our indications of wind-driven currents are for 0200 and 1400 h only. MAVEN data taken over the full range of local times will give a more complete view of ionospheric fields and enable a better comparison with the Earth Sq current. Nonetheless, we expect differences between the terrestrial and Martian fields. For example, due to the existing global magnetic dipole field on Earth, strongly enhanced magnitudes at the equator (the equatorial electro jet, EEJ) can be observed where the global geomagnetic field is close to horizontal. *Yamazaki and Maute* [2017] present a comprehensive review on Sq currents and the EEJ.

Non-zero mean current systems, such as wind-driven current sources or dayside compression of the IMF, have an effect on crustal field modeling, as they complicate the identification of purely lithospheric sources. Due to the wealth of data coverage provided by MGS mapping orbit and MAVEN data, we suggest that wherever possible, daytime data should be excluded in investigations of magnetic fields of lithospheric origin, as non-crustal sources with non-zero mean signals are present, have large-scale coherent spatial structure, and can reach tens of nanoteslas on average at 400 km altitude on the dayside. In addition, the temporal variability in such signals is large. On the nightside, the average non-crustal fields over many IMF cycles are small, however the temporal variability in such signals is still large. We also detect variability in the nightside data, although weaker, likely because ionospheric plasma densities are at least an order of magnitude lower [*Němec et al.*, 2011]. The MGS mapping orbit allows averaging of many orbits over a given geographical location and therefore provides robust estimates of the static lithospheric signal. However, when using daytime measurements or nighttime tracks without many repeat measurements, "noisy orbits" must be identified and excluded to avoid contamination of the lithospheric signal. This will be the case for data from MAVEN, because of its precessing orbit. *Langlais et al.* [2017] recently suggested a measure of activity which allows identification of orbits heavily influenced by external field conditions. External fields must therefore be carefully considered in future lithospheric field modeling.

4.2. Magnetic Sounding

Geophysical data sets are important to constrain the interior structure of Mars. To date, information on the Martian crust and mantle composition has been derived from SNC meteorite studies, combined with models and data of the interior based on gravity, topography, and shape [e.g., *Sohl and Spohn*, 1997]. Here we discuss the possibility of a further method for exploring the subsurface, specifically magnetic sounding. An external, time-varying magnetic field (the inducing field) can induce currents in the interior of the planet, which depend on the interior electrical conductivity structure. Conductivity, in turn depends on mineralogy, temperature and the presence of volatiles [*Hjelt and Korja*, 1993; *Tarits*, 1994]. A typical approach in satellite-based conductivity studies is to identify the spatial structure in the inducing field at specific periods [e.g., *Civet et al.*, 2015; *Kuvshinov*, 2012; *Olsen*, 1999], typically via a spherical harmonic expansion. For spherically symmetric interior conductivity models (i.e., only a function of radius) the induced field at each period is linearly related to inducing field through a transfer function that depends only on spherical harmonic degree and period.

The InSight lander will begin operations on the surface of Mars starting in late 2018. InSight carries a magnetometer that will measure the vector magnetic field continuously at 0.2 Hz and increased frequency during magnetic events. The time-varying magnetic field will comprise contributions from the lander and any naturally occurring time-varying fields including external (inducing) and induced fields. MAVEN will simultaneously measure the magnetic field and solar wind parameters from orbit. These combined observations will provide an opportunity for induction studies.

A good understanding of external fields is an important step in estimating the induced response and one that we can begin to address using our results here. We have shown that prominent periodicities in the inducing signal are the daily and 26-day periods. The 1-day and 26-day periods are important, as we expect to measure these periodicities multiple times over the full Martian year planned for InSight mission operations, enabling stacking of the data. This is important, as the induced signal is expected to be small compared to the inducing field, and both may be small compared to the time variable lander fields.

Using our earlier analysis, we subtract the nighttime data from the daytime data (shown in Figure 6) to obtain maps of the global-scale daily variation in the field averaged over 3 Mars years. We conduct a spherical harmonic expansion up to degree and order 5 of this field to get a large-scale model description of the daily variation in the global external field (Figure 6b). Correlation coefficients for the day-night difference field compared with the spherical harmonic model field are 0.44, 0.86, and 0.52 for B_r, B_θ, and B_φ, respectively. The model B_θ field captures the large-scale structure in the field well (Figure 6, middle row), whereas the smaller-scale patterns in B_r or B_φ are not captured in spherical harmonic degree and order 5 models. As previously discussed, the latter signals likely have a different physical origin from the large-scale zonal structure in B_θ.

Different periodicities carry information depending on skin or penetration depth, d, and conductivity, σ. We use approximate conductivity values expected for the crust (0.1 S/m) and mantle (10 S/m), respectively [*Mocquet and Menvielle*, 2000] and plot the simple relationship $d = \sqrt{\frac{1}{f\sigma\mu_0\pi}}$ (Figure 10), where f is the frequency of the external field variations. The daily and 26-day periods identified above provide a large range

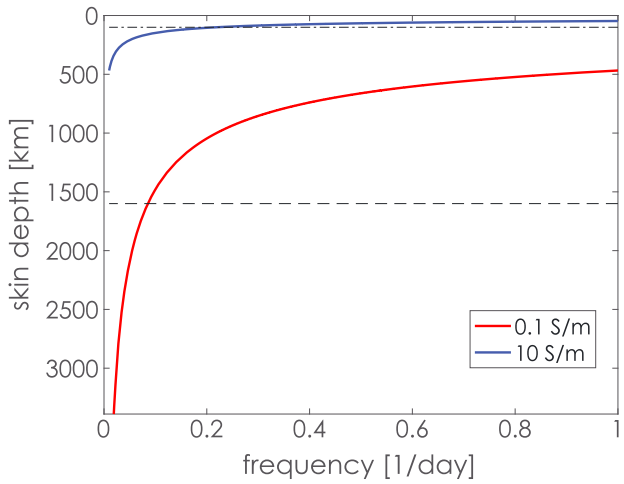

Figure 10. The skin depth versus frequency for the inducing field for different conductivities, σ, representing crust (0.1 S/m) and mantle (10 S/m). The dashed line indicates the approximate location of the core-mantle boundary. The dashed-dotted line represents the maximum crustal thickness of 100 km after *Wieczorek* [2007].

of depth information. In particular, the daily period and any higher frequency aperiodic signals [e.g., *Civet and Tarits*, 2014] sample the crust and upper mantle.

Several challenges still exist for magnetic sounding studies at Mars. First, for the InSight mission, removal of spacecraft fields from the magnetic field data will be essential—these may be the dominant signal and, in particular, will contain a daily signal arising from reduced operations during the nighttime compared with during the daytime. Second, it is unclear what the inducing signal will be at the surface because only a very few MGS and MAVEN orbits have measured the magnetic field below the ionospheric peak. However, the relatively limited number of dayside MGS orbits that have measured the magnetic field below the ionospheric peak show substantial variability [*Withers*, 2009]. The ionosphere is an internal field source, as seen from the MGS mapping orbit and most MAVEN orbits, whereas the IMF would be an external source. Altitude profiles of the magnetic field strength constructed from MGS data do not indicate a simple downward continuation from the IMF or upward continuation from the ionosphere indicating superposition of fields from multiple sources [*Mittelholz and Johnson*, 2016]. Understanding the spatial structure and frequency content of the external field below the ionosphere is an important avenue of future research.

5. Conclusion

We have investigated global external magnetic fields on Mars using the MGS mapping orbit data set from 2000 to 2006. We have identified periodic signals including daily, 26-day, and annual cycles. We identify three major contributions to the external field at satellite altitude. First, the alternating polarity of the draped, compressed IMF is clearly seen when data are stacked for each day in the 26-day Carrington rotation cycle. Second, some structure in the external field results from interaction with crustal fields as previously reported [*Acuña et al.*, 2001; *Brain et al.*, 2003]. Third, a contribution is observed that results in persistent dayside latitudinal structure in the field, irrespective of the IMF polarity or season. This zonal structure is seen clearly in the B_θ component of the field in the body-fixed frame. We suggest that this could result, at least in part, from ionospheric currents driven by winds in the upper atmosphere. We show that wind fields predicted by current Mars climate models can result in ionospheric currents and associated magnetic fields that have a direction and magnitude consistent with the observed structure in the field. The identified daily and 26-day periodicities in the external field, as well as large amplitude, aperiodic, solar events, and higher-frequency signals, offer the potential for interior electrical conductivity studies of the Martian crust and upper mantle [e.g., *Menvielle et al.*, 2000; *Civet and Tarits*, 2014] using data to be returned from the InSight mission.

Acknowledgments
This work was supported by the University of British Columbia, a Canadian Space Agency grant to C.L.J. to support PhD student .A.M, and an NSERC CREATE award to A.M. C.L.J. acknowledges InSight mission support to the Planetary Science Institute, and R.L.J. acknowledges MAVEN mission support to the University of California Berkeley Space Sciences Laboratory. The MGS magnetic field data used in this study are archived in the Planetary Data System, the crustal field spherical harmonic model, M14, is published in the supporting information of *Morschhauser et al.* [2014], and the MGCM model is available from http://www.mars.lmd.jussieu.fr/mars/access.html. We thank Alain Plattner and an anonymous reviewer for thoughtful comments that improved the manuscript.

References

Acuña, M. H., et al. (1998), Magnetic field and plasma observations at Mars: Initial results of the Mars Global Surveyor Mission, *Science*, *279*(5357), 1676–1680.

Acuña, M. H., et al. (1999), Global distribution of crustal magnetization discovered by the Mars Global Surveyor MAG/ER Experiment, *Science*, *284*(5415), 790–793, doi:10.1126/science.284.5415.790.

Acuña, M. H., et al. (2001), Magnetic field of Mars: Summary of results from the aerobraking and mapping orbits, *J. Geophys. Res.*, *106*(E10), 23,403–23,418, doi:10.1029/2000JE001404.

Arkani-Hamed, J. (2001), A 50-degree spherical harmonic model of the magnetic field of Mars, *J. Geophys. Res.*, *106*(E10), 23,197–23,208, doi:10.1029/2000JE001365.

Arkani-Hamed, J. (2002), An improved 50-degree spherical harmonic model of the magnetic field of Mars derived from both high-altitude and low-altitude data, *J. Geophys. Res.*, *107*(E10), 5083, doi:10.1029/2001JE001835.

Brain, D., F. Bagenal, M. H. Acuña, and J. Connerney (2003), Martian magnetic morphology: Contributions from the solar wind and crust, *J. Geophys. Res.*, *108*(A12), 1424, doi:10.1029/2002JA009482.

Brain, D., D. L. Mitchell, and J. S. Halekas (2006), The magnetic field draping direction at Mars from April 1999 through August 2004, *Icarus*, *182*(2), 464–473, doi:10.1016/j.icarus.2005.09.023.

Brain, D., et al. (2010), A comparison of global models for the solar wind interaction with Mars, *Icarus*, *206*(1), 139–151, doi:10.1016/j.icarus.2009.06.030.

Cain, J. C. (2003), An $n = 90$ internal potential function of the Martian crustal magnetic field, *J. Geophys. Res.*, *108*(E2), 5008, doi:10.1029/2000JE001487.

Chapman, S., and J. Stagg (1929), On the variability of the quiet-day diurnal magnetic variation at Eskdalemuir and Greenwich, *Proc. R. Soc. A*, *123*(791), 27–53.

Civet, F., and P. Tarits (2014), Electrical conductivity of the mantle of Mars from MGS magnetic observations, *Earth Planets Space*, *66*, 85.

Civet, F., E. Thébault, O. Verhoeven, B. Langlais, and D. Saturnino (2015), Electrical conductivity of the Earth's mantle from the first Swarm magnetic field measurements, *Geophys. Res. Lett.*, *42*, 3338–3346, doi:10.1002/2015GL063397.

Connerney, J. E. P., M. H. Acuña, P. J. Wasilewski, N. F. Ness, H. Reme, C. Mazelle, D. Vignes, R. P. Lin, D. L. Mitchell, and P. A. Cloutier (1999), Magnetic lineations in the ancient crust of Mars, *Science*, *284*(5415), 794–798.

Crider, D., D. Vignes, A. M. Krymskii, T. Breus, N. F. Ness, D. L. Mitchell, J. A. Slavin, and M. H. Acuña (2003), A proxy for determining solar wind dynamic pressure at Mars using Mars Global Surveyor data, *J. Geophys. Res.*, *108*(A12), 1461, doi:10.1029/2003JA009875.

Eastwood, J. P., D. A. Brain, J. S. Halekas, J. F. Drake, T. D. Phan, M. Øieroset, D. L. Mitchell, R. P. Lin, and M. H. Acuña (2008), Evidence for collisionless magnetic reconnection at Mars, *Geophys. Res. Lett.*, *35*, L02106, doi:10.1029/2007GL032289.

Ferguson, B. B., J. C. Cain, D. H. Crider, D. a. Brain, and E. M. Harnett (2005), External fields on the nightside of Mars at Mars Global Surveyor mapping altitudes, *Geophys. Res. Lett.*, *32*, L16105, doi:10.1029/2004GL021964.

Fillingim, M. O., R. J. Lillis, S. L. England, L. M. Peticolas, D. A. Brain, J. S. Halekas, C. Paty, D. Lummerzheim, and S. W. Bougher (2012), On wind-driven electrojets at magnetic cusps in the nightside ionosphere of Mars, *Earth Planets Space*, *64*(2), 93–103, doi:10.5047/eps.2011.04.010.

Forget, F., F. Hourdin, R. Fournier, C. Hourdin, O. Talagrand, M. Collins, S. R. Lewis, P. L. Read, and J.-P. Huot (1999), Improved general circulation models of the Martian atmosphere from the surface to above 80 km, *J. Geophys. Res.*, *104*(E10), 24,155–24,176, doi:10.1029/1999JE001025.

Halekas, J., and D. Brain (2010), Global distribution, structure, and solar wind control of low altitude current sheets at Mars, *Icarus*, *206*(1), 64–73, doi:10.1016/j.icarus.2008.12.032.

Hjelt, S. E., and T. Korja (1993), Lithospheric and upper-mantle structures, results of electromagnetic soundings in Europe, *Phys. Earth Planet. Inter.*, *79*(1–2), 137–177, doi:10.1016/0031-9201(93)90146-Z.

Kuvshinov, A. V. (2012), Deep electromagnetic studies from land, sea, and space: Progress status in the past 10 years, *Surv. Geophys.*, *33*(1), 169–209, doi:10.1007/s10712-011-9118-2.

Langlais, B., M. E. Purucker, and M. Mandea (2004), Crustal magnetic field of Mars, *J. Geophys. Res.*, *109*, E02008, doi:10.1029/2003JE002048.

Langlais, B., F. Civet, and E. Thébault (2017), In situ and remote characterization of the external field temporal variations at Mars, *J. Geophys. Res. Planets*, *122*, 110–123, doi:10.1002/2016JE005060.

Lillis, R. J., and D. A. Brain (2013), Nightside electron precipitation at Mars: Geographic variability and dependence on solar wind conditions, *J. Geophys. Res. Space Physics*, *118*, 3546–3556, doi:10.1002/jgra.50171.

Menvielle, M., et al. (2000), Contribution of magnetic measurements onboard NetLander to Mars exploration, *Planet. Space Sci.*, *48*(12–14), 1231–1247, doi:10.1016/S0032-0633(00)00106-9.

Millour, E., F. Forget, A. Spiga, L. Montabone, S. Lebonnois, S. R. Lewis, and P. L. Read (2015), The Mars climate database (v4.3). EPSC Abstracts vol. 10, EPSC2015-438, paper presented at European Planetary Science Congress 2015, Nantes, France, 27 Sep.–2 Oct.

Mittelholz, A., and C. L. Johnson (2016), Global-scale external fields at Mars measured at satellite altitudes: Preparation for magnetic sounding of the Martian interior, paper presented at 47th Lunar and Planetary Science Conference, The Woodlands Waterway Marriott Hotel and Convention Center, The Woodlands, Texas, 21–25 March.

Mocquet, A., and M. Menvielle (2000), Complementarity of seismological and electromagnetic sounding methods for constraining the structure of the Martian mantle, *Planet. Space Sci.*, *48*(12–14), 1249–1260, doi:10.1016/S0032-0633(00)00107-0.

Morschhauser, A., V. Lesur, and M. Grott (2014), A spherical harmonic model of the lithospheric magnetic field of Mars, *J. Geophys. Res. Planets*, *119*, 1162–1188, doi:10.1002/2013JE004555.

Němec, F., D. D. Morgan, D. A. Gurnett, and D. A. Brain (2011), Areas of enhanced ionization in the deep nightside ionosphere of Mars, *J. Geophys. Res.*, *116*, E06006, doi:10.1029/2011JE003804.

Olsen, N. (1999), Induction studies with satellite data, *Surv. Geophys.*, *20*(3–4), 309–340, doi:10.1023/A:1006611303582.

Olsen, N., K. H. Glassmeier, and X. Jia (2010), Separation of the magnetic field into external and internal parts, *Space Sci. Rev.*, *152*(1–4), 135–157, doi:10.1007/s11214-009-9563-0.

Owens, M. J., and R. J. Forsyth (2013), The heliospheric magnetic field, *Living Rev. Sol. Phys.*, *10*, 5, doi:10.12942/lrsp-2013-5.

Plattner, A., and F. J. Simons (2015), High-resolution local magnetic field models for the Martian South Pole from Mars Global Surveyor data, *J. Geophys. Res. Planets*, *120*, 1543–1566, doi:10.1002/2015JE004869.

Purucker, M., D. Ravat, H. Frey, C. Voorhies, T. Sabaka, and M. Acuña (2000), An altitude-normalized magnetic map of Mars and its interpretation, *Geophys. Res. Lett.*, *27*(16), 2449–2452, doi:10.1029/2000GL000072.

Sohl, F., and T. Spohn (1997), The interior structure of Mars: Implications from SNC meteorites, *J. Geophys. Res.*, *102*, 1613–1635.

Stone, E. C., A. M. Frandsen, and R. A. Mewaldt (1998), The advanced composition explorer, *Space Sci. Rev.*, *86*, 1–22, doi:10.1023/A:1005082526237.

Tarits, P. (1994), Electromagnetic studies of global geodynamic processes, *Surv. Geophys.*, *15*(2), 209–238, doi:10.1007/BF00689860.

Vogt, M. F., et al. (2016), MAVEN observations of dayside peak electron densities in the ionosphere of Mars, *J. Geophys. Res. Space Physics*, *121*, 891–906, doi:10.1002/2016JA023473.

Voorhies, C. V. (2008), Thickness of the magnetic crust of Mars, *J. Geophys. Res.*, *113*, E04004, doi:10.1029/2007JE002928.

Voorhies, C. V., T. J. Sabaka, and M. Purucker (2002), On magnetic spectra of Earth and Mars, *J. Geophys. Res.*, *107*(E6), 5034, doi:10.1029/2001JE001534.

Wieczorek, M. A. (2007), Gravity and topography of the terrestrial planets, *Treatise on Geophys.*, *10*, 165–206, doi:10.1016/B978-044452748-6/00156-5.

Withers, P. (2009), A review of observed variability in the dayside ionosphere of Mars, *Adv. Space Res.*, *44*(3), 277–307, doi:10.1016/j.asr.2009.04.027.

Yamazaki, Y., and A. Maute (2017), Sq and EEJ—review on the daily variation of the geomagnetic field caused by ionospheric dynamo currents, *Space Sci. Rev.*, *206*, 299–405, doi:10.1007/s11214-016-0282-z.